

## Relative permeability for two-phase flow through corrugated tubes as model porous media

Majid Ahmadiouydarab<sup>a</sup>, Zhong-Sheng (Simon) Liu<sup>b</sup>, James J. Feng<sup>a,c,\*</sup>

<sup>a</sup>*Department of Chemical and Biological Engineering, University of British Columbia,  
Vancouver, BC V6T 1Z3, Canada*

<sup>b</sup>*NRC Institute for Fuel Cell Innovation, 4250 Wesbrook Mall, Vancouver, BC V6T  
1W5, Canada*

<sup>c</sup>*Department of Mathematics, University of British Columbia, Vancouver, BC V6T 1Z2,  
Canada*

---

### Abstract

We report finite-element simulations of gas-liquid two-phase flows through a model porous medium made of corrugated tubes. By resolving the pore-scale fluid dynamics and interfacial morphology, we compute the relative permeability of the porous medium by averaging over a pore-size-distribution of a real porous medium. A constant pressure gradient is applied on both fluids to simulate a pressure-driven creeping flow, and a diffuse-interface model is used to compute the interfacial evolution and the contact line motion. We observe a number of flow regimes in the micropores, depending on the pore size, imposed pressure gradient and other geometric and physical parameters. The flow rates vary nonlinearly with the pressure gradient, and the extended Darcy's law does not hold in general. The interaction between the two phases, known as viscous coupling, is a prominent feature of the process. As a result, the relative permeability depends not only on saturation, but also on the capillary number, viscosity ratio, wettability of the solid wall, pore geometry, and the initial configuration. The effects of these factors are explored systematically and compared with previous studies.

*Keywords:* Interfacial flow, viscous coupling, pore-scale simulation, moving contact line, Cahn-Hilliard model, lubrication effect

---

\*Corresponding author

*Email address:* jfeng@chbe.ubc.ca (James J. Feng)

## 1. Introduction

Conventionally, two-phase flow in porous media is modeled by generalizing Darcy’s law into a linear relationship between the velocity and pressure gradient for each phase:

$$\mathbf{v}_i = \frac{\kappa \kappa_{r,i}}{\mu_i} \nabla p_i, \quad (1)$$

where  $\mathbf{v}_i$ ,  $p_i$ , and  $\mu_i$  are the velocity, pressure and viscosity of fluid  $i$ ,  $i = w$  or  $n$  for the wetting or nonwetting phase.  $\kappa$  is the intrinsic permeability of the porous medium, and  $\kappa_{r,i}$  is the *relative permeability* of phase  $i$ . This extended Darcy’s law is based on a physical picture of each phase flowing as if in a single-phase flow with the other phase serving only to reduce the size of the flow passage (Muskat and Meres, 1936). Fluid-fluid interaction across the interface is ignored, and  $\kappa_{r,i}$  is taken to be only a function of the average volume fraction in the pores, known as the saturation  $S$ .

Though appealing for its simplicity, the extended Darcy’s law has limited success in representing reality. For one, the two fluids generally do not follow bicontinuous pathways that remain invariant (Avraam and Payatakes, 1999). Instead, the interface evolves dynamically as a result of viscous and capillary forces, and undergoes morphological changes such as rupture and coalescence to produce slugs and bubbles (Ahmadlouydarab et al., 2011). Second, the hydrodynamic interaction between the two fluids introduces *viscous coupling* (Kalaydjian, 1990), such that the flow of one phase affects the other by viscous shearing, for example. Finally, *transient* flows, such as occur in water-oil displacement, produce temporal and spatial variations of the interface that cannot be predicted by the extended Darcy’s law (Avraam and Payatakes, 1999). Alternatively, Eq. (1) may be viewed as the definition of the relative permeabilities. Then  $\kappa_{r,i}$  must be understood as a convenient catchall into which all the complexities of the interfacial fluid dynamics have been lumped. Taking it to be a function of the saturation  $S$  alone is indefensible.

Then it comes as no surprise that measurement of  $\kappa_{r,i}(S)$  has produced not only large quantitative scatter but sometimes qualitative contradictions in the literature (Demond and Roberts, 1987). For instance, the assumption of separate, uncoupled single-phase flow implies  $\kappa_{r,n} + \kappa_{r,w} \leq 1$  (Demond and Roberts, 1987). This seems to be confirmed by some measurements (e.g. Dana and Skoczylas, 2002) but violated by others (e.g. Avraam and Payatakes, 1995a, 1999). Notably, Ehrlich (1993) and Yiotis et al. (2007) reported a  $\kappa_{r,n}$  that varies with  $S$  non-monotonically, with a maximum above

1 at an intermediate saturation. There are also long-running controversies over whether the interfacial tension and viscosity ratio between the two fluids affect the relative permeability (Amaefule and Handy, 1982; Demond and Roberts, 1987; Avraam and Payatakes, 1995a). A more general review of the experimental data can be found in Demond and Roberts (1987) and Avraam and Payatakes (1999).

An obvious interpretation of this discrepancy is that two-phase transport in porous media depends strongly on the interfacial morphology and fluid dynamics near the interface. In turn these depend on an array of parameters, including the volume fraction of the fluids, pore geometry, capillary number, wetting angle, viscosity ratio, and flow history (e.g., imbibition vs. drainage). Hence the relative permeabilities  $\kappa_{r,i}$  must be functions of these parameters as well. Several groups have explored the functional dependence of  $\kappa_{r,i}$  on such parameters, e.g., Demond and Roberts (1987); Avraam and Payatakes (1995b); Dana and Skoczylas (2002). In particular,  $\kappa_{r,n} > 1$  can be explained by *lubrication* of the high-viscosity non-wetting fluid by the less viscous wetting fluid (Yiotis et al., 2007). Gustensen and Rothman (1993) and Avraam and Payatakes (1995a, 1999) emphasized the importance of the interfacial morphology by correlating  $\kappa_{r,i}$  with the flow regimes, and Li et al. (2005) highlighted the special role of the interfacial area.

It is difficult to capture the interfacial morphology and flow behavior in real porous media. The pores typically have an irregular and complex geometry, and the solid is opaque. Direct flow visualization is therefore impossible. So far, experimental evidence on the flow field has come mostly from model porous media with regularized pore geometry. One particularly successful model is a 2D network of pore chambers and throats etched into glass (Avraam and Payatakes, 1995a, 1999), which made it possible to correlate  $\kappa_{r,i}$  with the interfacial flow. Similarly, computation of relative permeability has largely relied on simplified geometries, e.g. the tube bundle model (Ehrlich, 1993) and pore-network model (Blunt et al., 2002). Such calculations assume quasi-static interfaces and postulate local solutions based on Poiseuille flow, and thus do not account for interfacial dynamics.

Recently, more realistic pore-scale computation by solving the Navier-Stokes equations has become possible. Accurate pore-scale knowledge of the flow field and interfacial morphology would be the ultimate solution for two-phase transport in porous media. But there are formidable numerical challenges in such computations. First, the interface constitutes an inner boundary whose position has to be solved together with the Navier-Stokes

equations for both phases. Second, the interfacial curvature and interfacial force have to be accurately computed using high resolution. Otherwise the interfacial deformation is subject to large errors (Yue et al., 2004) and even numerical instabilities (Ye et al., 2001). So far, the lattice Boltzmann method has met with some success (e.g. Gustensen and Rothman, 1993; Li et al., 2005; Yiotis et al., 2007; Hao and Cheng, 2010). However, resolution of the interface remains a numerical bottleneck because the regular lattice precludes adaptive refinement at the interface.

In the present study, we propose an alternative method for computing the pore-scale flow and the relative permeability of a model porous media. By using a *diffuse-interface* representation and adaptive refinement of finite elements at the interface, we have developed a highly accurate computational toolkit for simulating interfacial flows (Yue et al., 2006b; Zhou et al., 2010), which has been successfully applied to a host of interfacial flow problems, including drop breakup and coalescence, jet breakup in microfluidic channels, interfacial encapsulation and compound drops (Yue et al., 2005, 2006a; Zhou et al., 2006; Yue et al., 2008; Gao and Feng, 2011). Most recently, Ahmadlouydarab et al. (2011) used this tool to construct two-phase flow regime maps in corrugated microchannels. By computing two-phase flows in a collection of such microchannels, the relative permeabilities can be evaluated by averaging over a prescribed pore size distribution. The strength of our method, compared with the lattice Boltzmann method, is the much higher resolution of the interfacial motion. The weakness is the relatively simple representation of the pore geometry. By systematically exploring the effects of saturation, capillary number, wetting angle, viscosity ratio and initial configuration, we have taken a step toward constructing a solid understanding of the interfacial hydrodynamics that underlies the relative permeability.

## 2. Problem setup and methodology

We imagine the porous medium as a collection of parallel tubes, each having periodic contraction and expansion as shown in Fig. 1. Compared with the real geometry, this model retains the change in cross-sectional area along a pore through chambers and throats, but neglects branching and connectivity between the pores. Based on the volume of the voids, an effective radius can be defined for each corrugated tube:

$$R_e = \left( \frac{R_c^2 L_c + R_t^2 L_t}{L_c + L_t} \right)^{1/2} = R_t \left( \frac{\alpha \beta^2 + 1}{\alpha + 1} \right)^{1/2}, \quad (2)$$

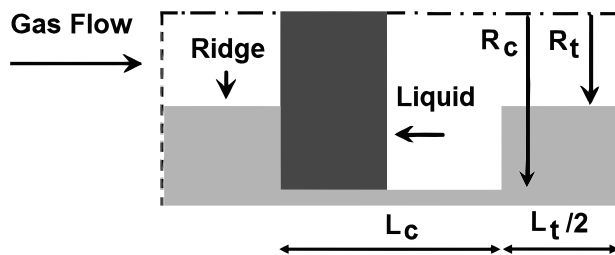


Figure 1: Schematics of the corrugated axisymmetric tube as a model for a pore. The computational domain is half of the meridian plane. The top of the domain is the axis of symmetry, and periodic boundary conditions are imposed between the left and right sides. The geometry is specified by three length ratios:  $\alpha = L_c/L_t$ ,  $\beta = R_c/R_t$  and  $\gamma = L_t/R_t$ , and we have used  $\alpha = 1$  and  $\beta = \gamma = 2$  for most of the computations. Initially the liquid forms a disc that blocks the cross-section of the groove representing the pore chamber.

where  $\alpha = L_c/L_t$  and  $\beta = R_c/R_t$  are length ratios. We assume that the collection of tubes is such that  $R_e$  obeys a prescribed pore size distribution (PSD). To impose a certain saturation  $S$  to our model porous medium, we fill each pore with both species of fluid to the prescribed  $S$ . This is a simplification since one may imagine larger and smaller pores carrying different volume fractions in reality. Now a pressure drop is applied to the porous medium, and a two-phase flow develops in each pore subject to the common pressure gradient. Because of the periodicity along the flow direction, the saturation in each pore stays fixed at  $S$ .

### 2.1. Averaging scheme

An averaging scheme is needed to compute macroscopic properties such as permeability from pore-scale flow quantities. In each tube, we compute the flow until a steady or periodic flow pattern is achieved; in the latter case, the time-averaged flow rate is obtained. To illustrate the averaging among the tubes, let us consider a single-phase flow first. The flow rate through a tube of radius  $R$  is:  $q = \pi R^2 u$ ,  $u$  being the average velocity through this tube. The total flow rate through the collection of tubes is, therefore:

$$Q = \int \psi(R)q dR, \quad (3)$$

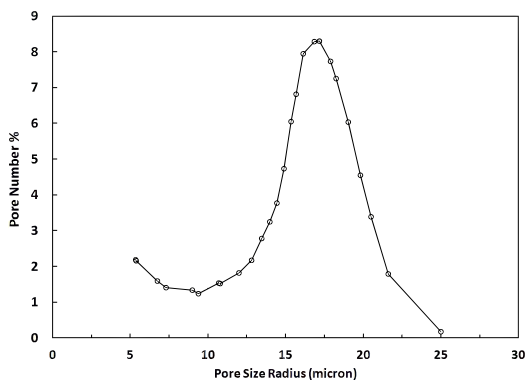


Figure 2: Pore size distribution (PSD) of a model porous medium. The distribution function  $\Psi(R)$  is converted from the data of Koido et al. (2008) on pore volume distribution.

where  $\psi$  is the PSD normalized such that  $\int \psi(R) dR = 1$ . As the total area  $A$  of the porous medium is related to the total pore area by the porosity  $\varphi$ :  $\varphi A = \int \psi(R) \pi R^2 dR$ , the average velocity over the entire porous medium can be computed:

$$v = \frac{Q}{A} = \frac{\varphi \int \psi(R) R^2 u dR}{\int \psi(R) R^2 dR}. \quad (4)$$

Now the intrinsic permeability of the model porous medium can be computed from  $v$  and the imposed pressure gradient:  $\kappa = \mu v / |\nabla p|$ ,  $\mu$  being the viscosity.

The same averaging scheme can be repeated for a two-phase flow simulation to yield the effective permeabilities for each phase. The ratio between the effective permeability and the intrinsic permeability gives the relative permeability for each phase. The porosity  $\varphi$  will cancel out and will not affect the relative permeability. But it does enter the average velocity for each phase and the capillary numbers. In all results to be presented, we have used the PSD of Fig. 2 for a gas diffusion layer (Toray TGP-H-060) of hydrogen fuel cells (Koido et al., 2008). The porosity for this porous medium,  $\varphi = 0.8$ , is used throughout the paper. Note that this value is larger than typical porosity in natural sandstones, and is specific to the engineered gas diffusion layer. The integrals in Eq. (4) are computed by summing over increments of the pore size; 25 pore sizes are computed in the range of 5.35–25  $\mu\text{m}$ , corresponding to the measured data points in Fig. 2.

## 2.2. Governing equations and numerical method

To solve the two-phase flow in the periodic axisymmetric domain of Fig. 1, we use a diffuse-interface formulation that accommodates evolving interfaces and moving contact lines in an energy-based framework. Various aspects of the theoretical model and numerical algorithms have been described at length elsewhere (Feng et al., 2005; Yue et al., 2006b; Zhou et al., 2010), and the current computations follow closely our recent study of two-phase flow regimes in corrugated microchannels (Ahmadlouydarab et al., 2011). Therefore, we will only list the governing equations below and briefly mention a few features of the numerical method.

A phase-field variable  $\phi$  is introduced such that  $\phi = 1$  in one fluid and  $\phi = -1$  in the other. The two-phase flow in the pore is described by the Navier-Stokes and Cahn-Hilliard equations:

$$\nabla \cdot \mathbf{u} = 0, \quad (5)$$

$$\nabla p = \nabla \cdot [\mu(\nabla \mathbf{u} + \nabla \mathbf{u}^T)] + G\nabla\phi + \mathbf{B}, \quad (6)$$

$$\frac{\partial\phi}{\partial t} + \mathbf{u} \cdot \nabla\phi = m\nabla^2 G, \quad (7)$$

where  $m$  is the Cahn-Hilliard mobility,  $G$  is the chemical potential and  $G\nabla\phi$  is the diffuse-interface representation of the interfacial tension.  $\mathbf{B}$  is a constant body force acting on both phases that represents the pressure gradient imposed over each periodic length of the pore:  $B = \Delta p/(L_c + L_t)$ . The effective viscosity  $\mu$  is defined as an average between that of the fluids weighted by the volume fractions  $(1 \pm \phi)/2$ . For typical flow in microscopic pores, the Reynolds and Bond numbers are much below unity (Zhang et al., 2006; Koido et al., 2008), and we have neglected inertia and gravity. The flow is thus governed by the external pressure gradient along with capillary and viscous forces.

The initial condition typically has the liquid and gas at rest in the domain of Fig. 1 with the desired saturation  $S$  and a certain initial configuration for the interface. Under the constant driving force  $B$ , both components start to flow and eventually a steady, time-periodic or quasi-periodic flow pattern establishes itself. Periodic boundary conditions are imposed between the left and right ends of the computational domain, and symmetry conditions on the top of the domain. On the solid substrate, no-slip conditions are used for velocity, and contact line motion is implemented via Cahn-Hilliard diffusion (Yue et al., 2010). The contact angle is introduced via surface

energies between each fluid and the solid (Yue et al., 2010; Yue and Feng, 2011).

The dimensionless parameters of the problem include an effective Bond number  $F = BL^2/\sigma$ , which indicates the ratio between the driving force and the surface tension, the saturation  $S$ , non-wetting to wetting phase viscosity ratio  $M = \mu_n/\mu_w$ , contact angle  $\theta$  and the length ratios  $\alpha$ ,  $\beta$  and  $\gamma$ . The length scale  $L$  will be specified below. A capillary number  $Ca$  can be defined for each phase using its average velocity (Eq. 4):  $Ca_i = \mu_i v_i/\sigma$ . But this will be an outcome of the simulation, not a control parameter. The results consist mainly of the relative permeabilities as functions of these parameters.

The governing equations are solved using finite elements on an unstructured triangular grid. The grids near the fluid interface are adaptively refined and coarsened as the interface moves. An implicit time-marching scheme is used, with Newton iterations at each time step. The algorithm has been validated previously using drop motion problems as benchmarks (Yue et al., 2006b; Zhou et al., 2010). For the specific setup here, Ahmadlouydarab et al. (2011) have done mesh-refinement tests to ensure that the numerical results have converged with the grid size.

### 3. Results and discussions

We have chosen a problem setup with a set of baseline parameters:  $\alpha = 1$ ,  $\beta = 2$  and  $\gamma = 2$ , wetting angle  $\theta = 135^\circ$ , and viscosity ratio  $M = 18$ . The  $\theta$  and  $M$  values correspond to typical operating conditions in the gas diffusion layer (GDL) of PEM fuel cells, with water and air at  $80^\circ\text{C}$ . The solid wall is hydrophobic; water is the non-wetting phase while air is the wetting phase. For convenience, we will refer to the non-wetting phase as water or liquid, and to the wetting phase as air or gas. The conclusions drawn, of course, will be general and not restricted to this specific pair of fluids. In the following,  $S$  or “saturation” refers to that of the liquid, i.e. non-wetting, phase. Initially a liquid bridge of thickness  $L_c/2$  occludes the pore chambers entirely (Fig. 1). This initial setup gives a liquid saturation  $S = 40\%$ , which will remain fixed throughout each computation. In the subsections to follow, we will vary one of the parameters to examine its effects while keeping the other parameters at their baseline values.

Since our porous medium consists of tubes of different sizes, and the same effective body force  $B$  is applied to all of them, the flow regime varies among the tubes. This is conveniently indicated by a local Bond number

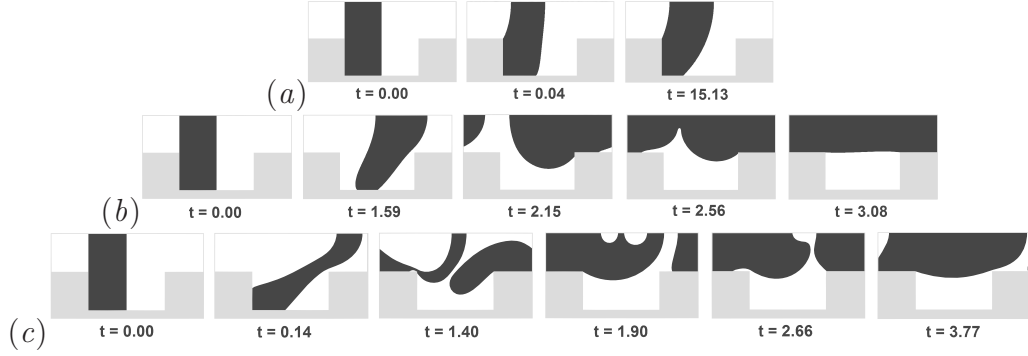


Figure 3: Temporal development of three flow regimes for the baseline parameter values: length ratios  $\alpha = 1$ ,  $\beta = 2$ ,  $\gamma = 2$ ; liquid-gas viscosity ratio  $M = 18$ , liquid saturation  $S = 40\%$  and wetting angle  $\theta = 135^\circ$ . Time is scaled by  $\mu_n R_e / \sigma$ . (a) Blockage at  $F_R = 0.38$ , when the imposed pressure fails to dislodge the liquid bridge pinned at the corner of the pore chamber; (b) liquid flow regime at  $F_R = 0.56$ , with the gas entirely trapped in the pore chamber; (c) drop flow regime at  $F_R = 1.4$ , with large liquid drops being surrounded and conveyed by a continuous gas phase.

$F_R = BR_e^2 / \sigma$  defined for each tube. A number of flow regimes have been observed with increasing  $F_R$ : blockage, gas flow, liquid flow, bubble-slug, shell, annular and drop flow. Three of these are illustrated in Fig. 3. Note that the flow regimes are sensitive to the pore geometry and initial configuration (see Sec. 3.5). A more detailed description of the regimes and the temporal evolution of the interfacial morphology can be found in our previous study (Ahmadlouydarab et al., 2011).

Once we have detailed flow data, we compute the relative permeability  $\kappa_{r,n}$  and  $\kappa_{r,w}$  from Eq. (1) by averaging over the PSD of a model GDL (Fig. 2). In this context, it is necessary to have an overall Bond number  $F = BL^2 / \sigma$ , in which the characteristic length is chosen to be  $L = 18.25 \mu\text{m}$ , the effective pore radius corresponding to the maximum of the PSD of Fig. 2, that is, the effective radius of the most common pore size. Now the relative permeabilities should be complex functions of the flow parameters (Avraam and Payatakes, 1995b):

$$\kappa_{r,i} = \kappa_{r,i}(S, Ca_n, Ca_w, M, \theta). \quad (8)$$

In addition,  $\kappa_{r,i}$  may depend on the geometrical parameters, initial configuration and flow history. In our setup, the key control parameter is actually

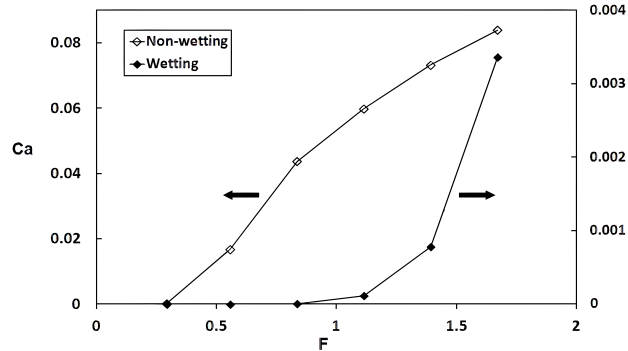


Figure 4: Dependence of the liquid and gas capillary numbers on the driving force  $F$ . All other parameters are at the baseline values given in Fig. 3.

the driving force  $F$ ; the capillary numbers for the flow  $Ca_i$  come out as a result. We list  $Ca_i$  instead of  $F$  in keeping with the conventional protocol in the literature.

### 3.1. Capillary number effect

The premise for Darcy’s law is the linearity between the flow rate and the imposed pressure drop. In single-phase, inertialess flow this holds. A fluid interface that deforms according to viscous and capillary forces introduces a geometric nonlinearity into the problem, and it is important to see if this compromises the linearity underlying the extended Darcy’s law. We vary the imposed body force  $B$  and compute the average velocity of each phase and a capillary number:  $Ca_i = \mu_i v_i / \sigma$ . Figure 4 plots the liquid and gas capillary numbers as functions of  $F$ .

For both phases, the variation of  $Ca$  with  $F$  is decidedly nonlinear. For  $F < 0.29$ , the blockage regime prevails even in the largest pores, with neither phase moving (cf. Fig. 3a). With increasing  $F$ , *capillary breakthrough* takes place first in the largest pores (Djilali, 2007). This causes a transition to the liquid flow regime (Fig. 3b), and produces a positive  $Ca_n$  for the non-wetting liquid phase. The gas is still trapped in the pore chambers by the liquid at this stage. Gas flow starts around  $F = 0.84$ , when the liquid core breaks up into drops, liberating the gas pocket in the largest pores and causing a transition to the drop flow regime (Fig. 3c). Increasing  $F$  further activates gas flow in smaller pores, and causes  $Ca_w$  to rise sharply. For even larger  $F$ , the drop flow regime prevails in most pores; further increase in  $F$  reduces

the size of the liquid drops but produces no new flow regimes. Since the gas is much less viscous than the liquid,  $Ca_w$  increases more steeply with  $F$  than  $Ca_n$ . Based on the above, it is obvious that the evolution of interfacial morphology makes the overall flow nonlinear in the porous medium.

It is interesting to compare our result with the lattice-Boltzmann computations of Gustensen and Rothman (1993). First, they have also observed a blockage regime at weak forcing and a subsequent breakthrough. However, they adopted a smoothed geometry with no interfacial pinning, and started from a core-annular initial morphology with the non-wetting fluid enveloped by the wetting one (see their Fig. 10). In their setup, therefore, it is the *non-wetting* species that is blocked at weak forcing. This comparison helps to illustrate the important role of the pore geometry and the initial configuration, which will be examined at greater length in Sec. 3.5. Furthermore, they have recognized that the evolving interfacial morphology produces a nonlinear  $Ca \sim F$  relationship, in qualitative agreement with our simulation. Finally, in the limit of strong forcing, they predicted drop flow for  $S = 10\%$  and annular flow for  $S = 30\%$ . These regimes have been seen in our simulations as well [see phase diagram in Ahmadlouydarab et al. (2011)]. Interestingly, Gustensen and Rothman (1993) observed that the  $Ca \sim F$  relationship becomes more or less linear in this limit, since the two phases are flowing roughly in stratified layers with less coupling. This can also be said of our drop flow regime of Fig. 3(c). Therefore, a fast linear regime may exist in our Fig. 4 as well, though our data do not range to sufficiently large  $F$  values to provide clear evidence.

The same nonlinearity can be illustrated by plotting the relative permeability of each phase as a function of their respective capillary number (Fig. 5). As expected,  $\kappa_{r,i}$  is not a constant; it varies appreciably with the flow. This is particularly true for the wetting phase. The nearly linear rise of  $\kappa_{r,w}$  with  $Ca_w$  mirrors the sharp upturn in Fig. 4; in the drop flow regime the gas transport increases more rapidly with increasing driving force than the liquid transport. For the non-wetting liquid phase, the initial rise of  $\kappa_{r,n}$  with  $Ca_n$  is due to the progressive formation of a liquid core lubricated by a gas pocket in the pore chamber, similar to Fig. 3(c). For higher  $Ca_n$ ,  $\kappa_{r,n}$  saturates because even in the smaller pores, the liquid becomes fully insulated from the solid wall by a gas cushion, and lubrication cannot be further enhanced. That  $\kappa_{r,n}$  is nearly flat for  $Ca_n > 0.04$  is consistent with the near linearity of Fig. 4(a) for larger  $Ca_n$ , and can be likened to the fast linear flow regime of Gustensen and Rothman (1993) mentioned above.

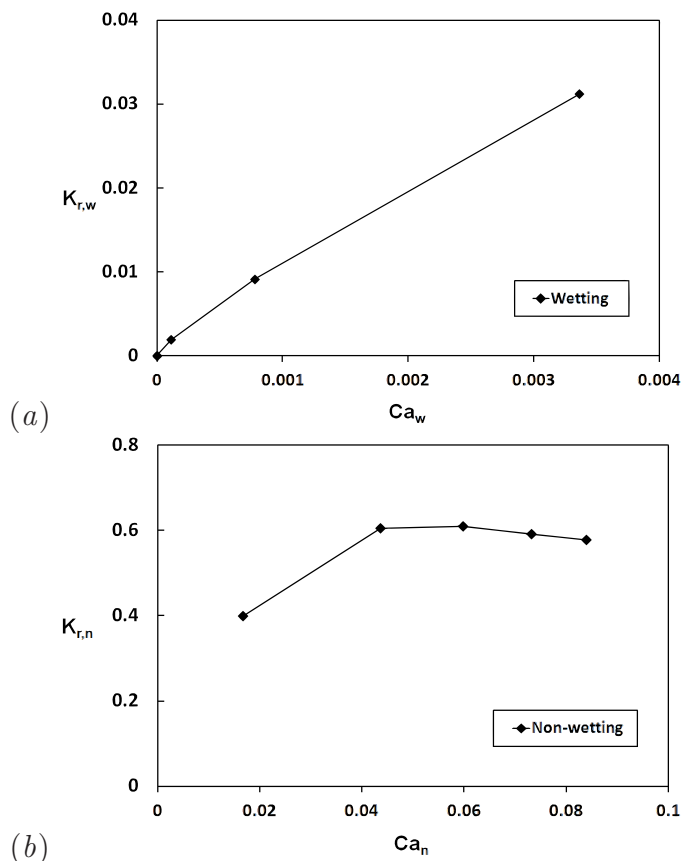


Figure 5: Variation of the relative permeability of (a) the wetting (gas) phase and (b) the non-wetting (liquid) phase with the respective capillary number. All other parameters are at the baseline values given for Fig. 3.

### 3.2. Saturation effect

To study the effect of the saturation level on the relative permeability, we use the same baseline geometry as illustrated in Fig. 1. By varying the initial thickness of the liquid bridge, we have computed liquid saturation  $S$  ranging from 10% to 80%. Figure 6 plots  $\kappa_{r,i}$  as functions of  $S$ . Note that in our setup, the liquid is the non-wetting phase.

In straight pores, it is intuitive to think that increasing the liquid saturation will increase the liquid-phase permeability and decrease the gas-phase permeability. In our geometry with pore throats and chambers, this intuition is mostly valid for the gas phase but not for the liquid. This can be

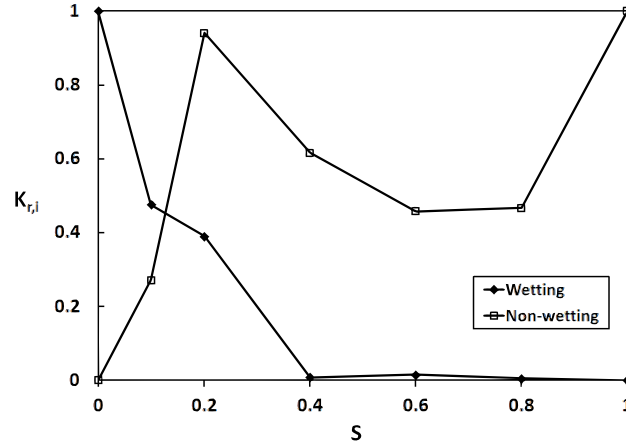


Figure 6: Relative permeabilities as functions of the liquid (non-wetting) saturation  $S$ .  $F = 1.4$  and all other parameters are at their baseline values given for Fig. 3.

understood from the flow regimes appearing in pores of different sizes at different saturations. We refer the reader to our earlier paper (Ahmadlouydarab et al., 2011) for images of the various flow morphologies cited below. At low saturation levels  $S < 20\%$ , the drop flow regime prevails in almost all pores. Thus, increasing  $S$  leads to larger drops that flow in the central part of the pore, being lubricated by a gas layer that separates the drops from the solid walls. As a result, the liquid permeability  $\kappa_{r,n}$  increases and the gas permeability  $\kappa_{r,w}$  decreases with  $S$ . In this range, the behavior is consistent with convention in the literature (Demond and Roberts, 1987). Beyond  $S = 20\%$ , the liquid drops become larger and start to come into contact with the solid walls, especially in the smaller pores. This significantly suppresses the lubrication effect. Some of the liquid may even be trapped in the pore chamber and excluded from the liquid throughput altogether. The dominant flow regime becomes bubble-slug flow. Consequently,  $\kappa_{r,n}$  declines with  $S$ . Meanwhile, in the smallest pores the gas starts to be entrapped in the pore chambers by liquid. Thus  $\kappa_{r,w}$  continues its decline. For  $S > 40\%$ , gas flux is maintained only in the largest pores, in the form of gas bubbles carried by a continuous liquid stream. In this stage, the liquid permeability levels off and becomes insensitive to  $S$ . Finally, as  $S \rightarrow 1$ , the gas bubbles shrink and eventually disappear;  $\kappa_{r,n}$  climbs back to unity.

The distinctive features of  $\kappa_{r,i}$  seen in our simulations are closely related to

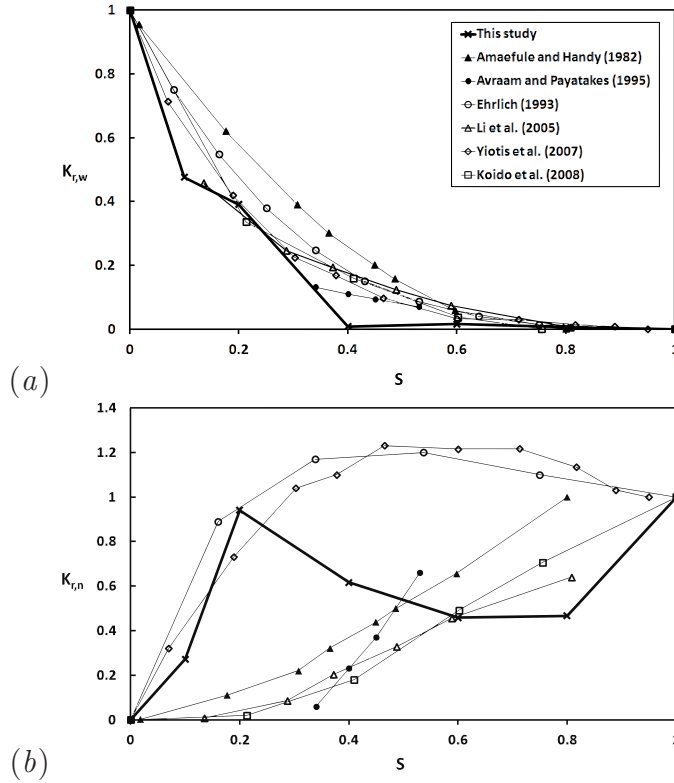


Figure 7: Comparison of the relative permeabilities  $\kappa_{r,i}(S)$  with previous studies. (a)  $\kappa_{r,w}$  of the wetting phase; (b)  $\kappa_{r,n}$  of the non-wetting phase. Open symbols denote computational results while closed ones experimental results. For our result, the body force  $F = 1.4$  and the other parameters are the same as in Fig. 3.

the geometry of our model porous medium. The interfacial morphology and flow regimes have much to do with interface pinning at sharp corners and with initial layout of the interface. Such detailed characteristics have not been recorded in prior experiments and computations. It is therefore particularly interesting to compare our results with prior studies. There is a wealth of experimental and numerical data in the literature on  $\kappa_{r,i}$  as functions of  $S$ , as the saturation is the parameter most thoroughly studied. Unfortunately, there are great variations in the values of other parameters, which make quantitative comparison very difficult. We have collected in Fig. 7 what appear to be reliable and representative data sets for a comparison with our numerical results.

All studies have produced a  $\kappa_{r,w}$  in close agreement with one another. In general, the gas permeability  $\kappa_{r,w}$  decreases with  $S$ , which in our convention denotes the saturation of the liquid, non-wetting phase. This robust trend can be attributed to the gradual narrowing of flow areas available to the gas with increasing  $S$ . Our  $\kappa_{r,w}$  being relatively low may be because in our geometry, the gas tends to be trapped in the pore chamber in certain flow regimes.

For  $\kappa_{r,n}$ , there are much greater variations in the data. Previous results seem to segregate into two groups: the tube-bundle (Ehrlich, 1993) and pore-network models (Yiotis et al., 2007) predict a higher  $\kappa_{r,n}$  that exceeds unity, while lattice-Boltzmann computations in random porous media (Li et al., 2005; Koido et al., 2008) and experiments (Amaefule and Handy, 1982; Avraam and Payatakes, 1995a) give a much lower  $\kappa_{r,n}$  that increases monotonically with  $S$ . Our prediction falls into the first group for smaller  $S$ , and then crosses over to the second for larger  $S$ . In the first group, the larger  $\kappa_{r,n}$  is clearly due to lubrication. In relatively simple geometries, stratification of the two phases occurs more consistently than in tortuous and random flow conduits. Besides, the lubrication effect is accentuated by a high non-wetting-to-wetting viscosity ratio  $M$ , which happens to be the case in the first group of studies ( $M \sim 10$  compared with  $M \sim 1$  for the second group). These conspire to produce the higher  $\kappa_{r,n}$ . With increasing  $S$ , the water tends to touch the solid wall at the pore throat as mentioned above. This hampers lubrication and causes our  $\kappa_{r,n}$  to decrease and join the second group of curves. In general, one can summarize the  $\kappa_{r,n}$  data as follows. The non-wetting phase typically stays away from the solid walls, and its interfacial morphology is more sensitive to material and flow parameters than for the wetting phase. Hence, its relative permeability exhibits greater variation among different studies.

### *3.3. Wettability effect*

Wettability of the pores is an important determinant of the relative permeabilities. This property affects the interfacial morphology and, if a three-phase contact line appears, how fast the contact line moves on the walls. To examine this effect in our pore-scale calculations, we have used the same baseline setup (Fig. 1) and tested four values of the contact angle  $\theta$  from  $60^\circ$  to  $165^\circ$ . Figure 8 depicts the variation of  $\kappa_{r,i}$  with  $\theta$ . The main finding is that by making the pores more hydrophobic, with increasing  $\theta$ , both relative permeabilities tend to decrease up to  $\theta = 135^\circ$ . With further increase in  $\theta$ ,

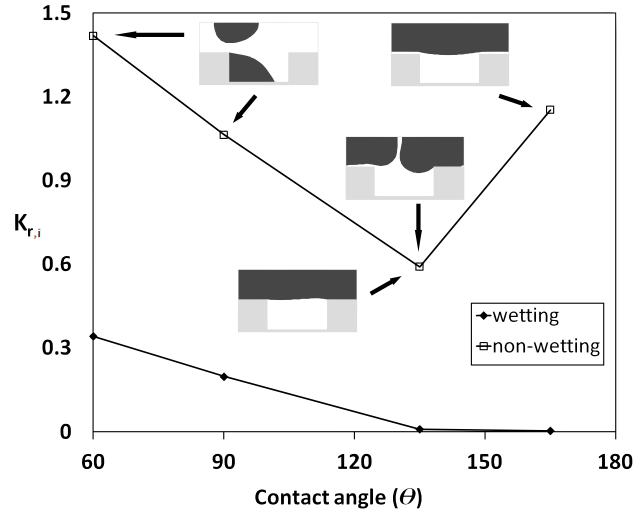


Figure 8: Relative permeabilities as functions of the liquid wetting angle  $\theta$  on the solid surface.  $F = 1.4$ , and the other parameters are at the baseline values of Fig. 3. The wetting and non-wetting phases refer respectively to the gas and liquid, regardless of the  $\theta$  value. The insets show dominant flow patterns among the pores responsible for the overall  $\kappa_{r,i}$ .

the liquid relative permeability  $\kappa_{r,n}$  increases while that for gas  $\kappa_{r,w}$  stays near zero. Note that for  $\theta \leq 90^\circ$ , the liquid becomes the wetting phase. For simplicity, however, we have not switched the subscript in Fig. 8;  $\kappa_{r,n}$  refers to the liquid and  $\kappa_{r,w}$  to the gas regardless of  $\theta$ .

If the solid is hydrophilic ( $\theta < 90^\circ$ ), the smaller pores are blocked by a liquid meniscus, but the dominant flow regime in larger pores is the liquid drop regime depicted by insets in the figure. Some liquid is retained in the pore chamber, while the rest is carried by the gas as large drops in the center of the pore. The liquid phase enjoys a large  $\kappa_{r,n}$  because of this lubrication effect. Its decline from  $\theta = 60^\circ$  to  $135^\circ$  has to do with the narrow pore throat in our geometry. With increasing  $\theta$ , more liquid is initially driven out of the pore chamber. It then makes contact with the wall in the throat and thus suppresses lubrication by the underlying gas. As a result,  $\kappa_{r,n}$  decreases. While hydrophobicity rejects the liquid from the near-wall regions, the gas is increasingly pushed into the pore chambers. As a result, the gas permeability  $\kappa_{r,w}$  continues to decline. At  $\theta = 135^\circ$ , the liquid tends to seal

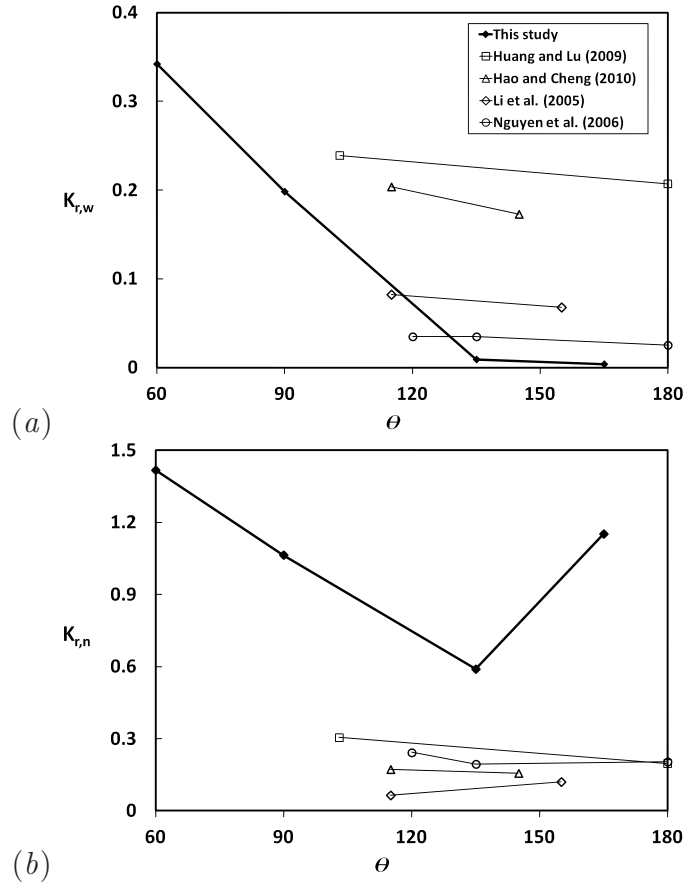


Figure 9: Effect of the contact angle  $\theta$  on the relative permeabilities  $\kappa_{r,w}$  (a) and  $\kappa_{r,n}$  (b): comparison with lattice-Boltzmann computations in the literature.

the gas completely in the chamber for smaller pores (lower inset) or to form liquid slugs separated by thin gas films in the larger pores (upper inset). The gas permeability approaches zero. At even higher  $\theta$ , the liquid-solid contact becomes so energetically prohibitive that the liquid starts to detach from the wall, allowing a gas film to wedge in between. In the end, the *shell flow* regime prevails in most of the pores, as illustrated by the inset for  $\theta = 165^\circ$ , with a liquid core enveloped by a thin gas sheath. This leads to the observed recovery of  $\kappa_{r,n}$ , again thanks to the lubrication effect.

Figure 9 compares our prediction of the wettability effect with several lattice-Boltzmann computations. We have found no clear-cut experimental

results; those that changed  $\theta$  by using different materials typically had other parameters changed as well. Among the lattice-Boltzmann computations, the geometry ranges from relatively regular (pore-network) to highly random. The physical parameters differ widely as well. For  $\kappa_{r,w}$ , the qualitative trend is the same for all studies:  $\kappa_{r,w}$  decreases with  $\theta$ . Note, however, that the prior computations are limited to relatively large  $\theta$ , where the decrease of  $\kappa_{r,w}$  with  $\theta$  is mild. Our computation includes smaller  $\theta$  where the effect is stronger. The difference in the numerical values among different studies has probably stemmed from the different physical and geometric parameters.

For  $\kappa_{r,n}$ , the picture is somewhat murkier. Li et al. (2005) showed  $\kappa_{r,n}$  to increase with  $\theta$ , Huang and Lu (2009) and Hao and Cheng (2010) predicted a mild decrease, while Nguyen et al. (2006) showed a non-monotonic trend. Our  $\kappa_{r,n}$  first decreases and then increases with  $\theta$ , and the magnitude is also much higher than the others. This can be attributed to our geometric and physical parameters amplifying the lubrication effect. For example, among the studies that have given the viscosity ratio  $M$ — $M = 1$  in Li et al. (2005), 12 in Huang and Lu (2009) and 18 in our study— $\kappa_{r,n}$  increases with  $M$ . This is due to the smaller friction on the non-wetting phase when the wetting phase viscosity is reduced (more on this in the next subsection). Besides, our geometry is regular and lacks tortuosity and cross-linkage among pores. It is well-known that lubrication effect is dampened in more complex and disordered pore geometry (Yiotis et al., 2007).

### 3.4. Viscosity ratio effect

The viscosity ratio affects the relative permeabilities mainly through lubrication effect. This has been noted in experiments (Avraam and Payatakes, 1995a) and computations in relatively simple geometries (Ehrlich, 1993; Yiotis et al., 2007). We have used our baseline setup of Fig. 1 and computed a range of the viscosity ratio, from  $M = 0.2$  to 18. Recall that  $M$  is the viscosity ratio between the non-wetting (liquid) and the wetting (gas) phase. Figure 10 shows that  $\kappa_{r,n}$  increases monotonically with  $M$  while  $\kappa_{r,w}$  decreases, both leveling off for large  $M$ . As explained below, this result confirms the key role played by lubrication effect.

Since the relative permeability for each phase is computed using its own viscosity (Eq. 1), it is convenient to think of the  $M$  effect as due to changing the viscosity of the other phase. For instance, the increase of the liquid permeability  $\kappa_{r,n}$  with  $M$  can be viewed as due to the gas viscosity getting lower. As  $\kappa_{r,i}$  are computed by averaging over potentially different flow regimes in

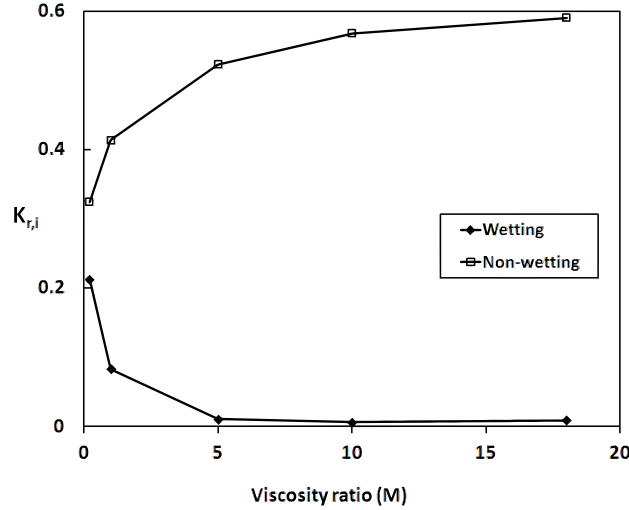


Figure 10: Relative permeabilities as functions of the liquid-gas viscosity ratio.  $F = 1.4$  and all other parameters are at the baseline values as given for Fig. 3.

pores of different sizes, it is not easy to rationalize the variations of  $\kappa_{r,i}$  in terms of the flow patterns. However, a qualitative argument can be made by looking at the flow regime in the *dominant pore sizes* in the PSD, roughly between 15 and 20  $\mu\text{m}$ . Figure 11 depicts the flow pattern in a pore of radius  $R_t = 18.25 \mu\text{m}$  for increasing  $M$  values. For smaller  $M$  values, shell flow prevails. Reducing the wetting-phase viscosity enhances the lubrication of the non-wetting fluid in the center. Hence  $\kappa_{r,n}$  increases with  $M$ . The same effect is at work in the annular-droplet regime for larger  $M$ , with the liquid above the gas pocket being lubricated, although quantitatively it is not as pronounced.

Similarly, in analyzing the gas-phase relative permeability  $\kappa_{r,w}$ , we imagine that  $M$  is being increased by raising the liquid viscosity while the gas viscosity remains constant. As  $M$  increases from 0.2 to 1, Fig. 11 indicates a transition from the shell-flow to the bubble-slug regime. This traps gas in the pore chamber and reduces  $\kappa_{r,w}$  sharply; all gas transport now occurs in the form of bubbles. With further increase in  $M$ , not only do the gas bubbles become smaller, but their velocity also decreases with increasing liquid viscosity. This explains the decline of  $\kappa_{r,w}$  with  $M$ .

The effect of the viscosity ratio on the relative permeability is an issue

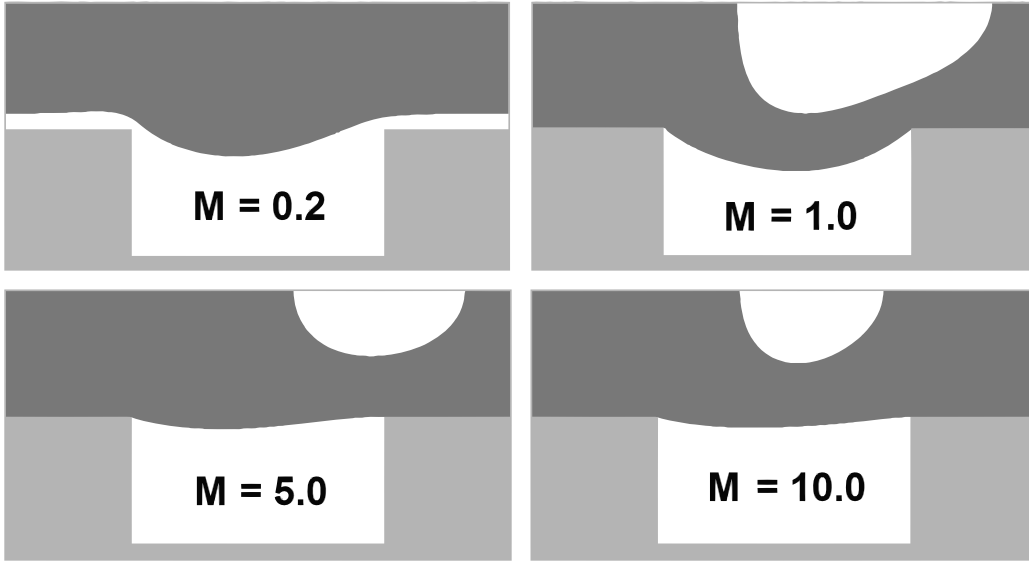


Figure 11: Flow patterns in a pore of radius  $R_t = 18.25 \mu\text{m}$  for increasing  $M$  values. Shell flow prevails for  $M = 0.2$  while bubble-slug flow obtains for larger  $M$ . All other parameters are at the baseline values as given for Fig. 3.

of some controversy in the literature (Demond and Roberts, 1987). Prior experiments and computations have been done at widely different values for the contact angle, saturation and capillary number. Nevertheless, we have compiled some data in Fig. 12 for a qualitative comparison. All computations, including ours, show a common trend that  $\kappa_{r,w}$  decreases with  $M$  while  $\kappa_{r,n}$  increases. This is mostly due to lubrication, although the effect should be tempered in real porous medium by the disordered nature of pore geometry (Yiotis et al., 2007). The two experiments do not agree with the computational trend. Amaefule and Handy (1982) showed both  $\kappa_{r,i}$  to decrease with  $M$  while Avraam and Payatakes (1995a) showed both to increase with  $M$ . We do not have an explanation for this discrepancy. Clearly more computational and experimental data are needed for a coherent picture to emerge.

### 3.5. Effects of pore geometry and initial configuration

Aside from the factors considered so far, Ahmadlouydarab et al. (2011) have demonstrated that the interface morphology and flow regimes are also

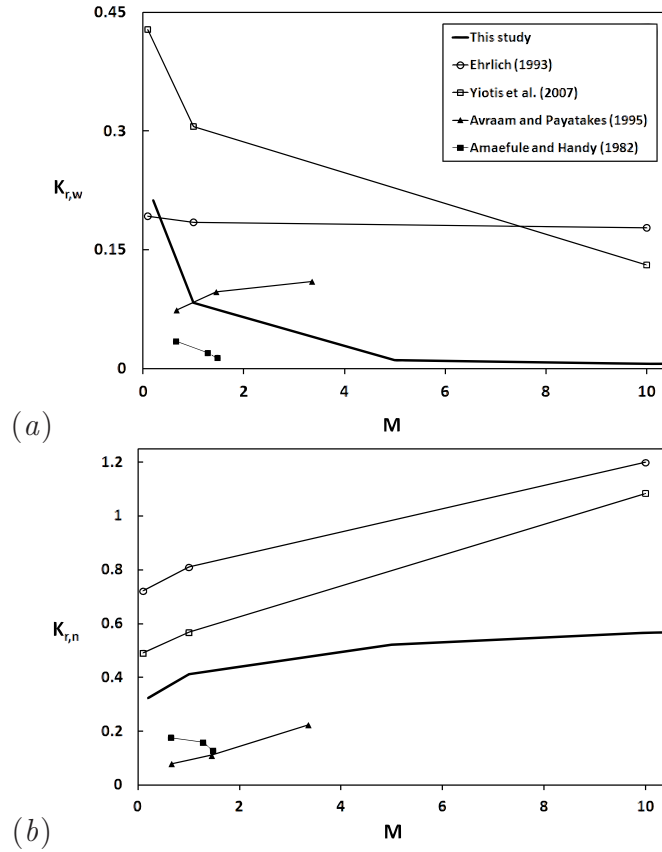


Figure 12: Comparison of (a)  $\kappa_{r,w}$  and (b)  $\kappa_{r,n}$  as functions of the viscosity ratio  $M$  with previous studies. Open symbols denote computations and filled ones experiments.

sensitive to the pore geometry and the initial configuration. For one, sharp corners tend to pin interfaces. This gives rise to very strong hysteresis in flow regimes, i.e. dependence on initial condition and flow history. Consequently, the relative permeability is expected to depend on these as well (Avraam and Payatakes, 1995a). Ahmadlouydarab et al. (2011) have examined these effects in considerable detail by varying the initial configurations and approaching a given flow condition by ramping up or down the flow rate. In the following we will briefly explore their ramifications for the relative permeabilities.

Figure 13 compares flow in micro-pores with sharp and rounded corners

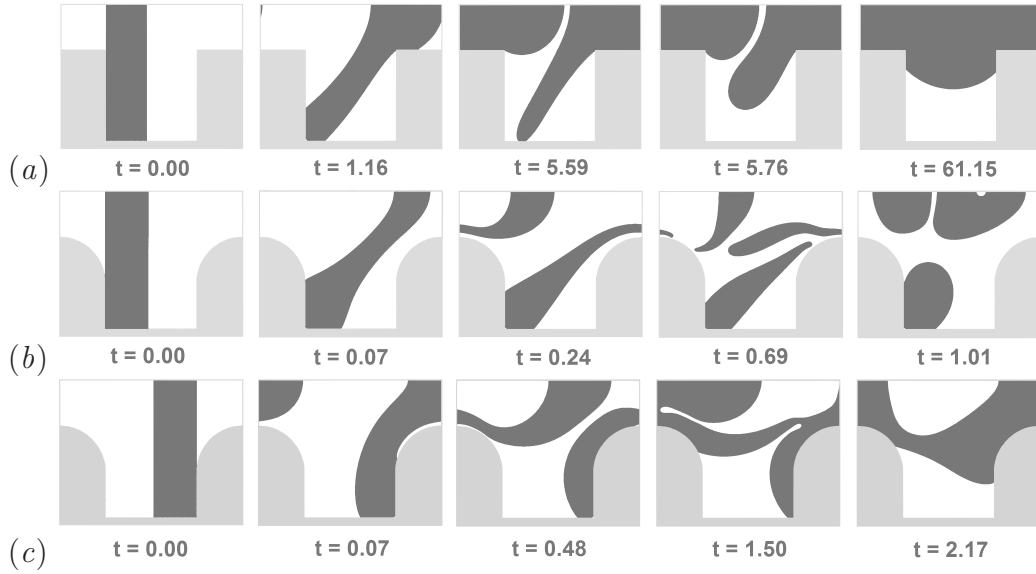


Figure 13: Effect of pore geometry and initial interfacial configuration. (a) Pore with sharp corners and the liquid bridge initially at the upstream end of the pore chamber. (b) Pore with rounded corners and the liquid bridge initially at the upstream end of the pore chamber. (c) Pore with rounded corners and the liquid bridge initially at the downstream end of the pore chamber. The parameters are the same for all three cases: effective pore radius  $R_e = 20 \mu\text{m}$ ,  $\alpha = 1$ ,  $\beta = 3$ ,  $\gamma = 2$ ,  $S = 40.5\%$ ,  $F_R = 1.4$ ,  $\theta = 135^\circ$  and  $M = 18$ .

(a and b), and in the latter case, two different initial positions for the liquid bridge (b and c). In Fig. 13(a), interface pinning at the two sharp corners slows down the movement of the liquid core and allows time for all the liquid to be drawn out of the pore chamber. In the end the liquid flow regime emerges, with the gas completely trapped in the pore chamber. In comparison, the flow develops much more rapidly with the rounded corners (Fig. 13b), leading to the drop flow regime. To evaluate  $\kappa_{r,i}$  for pores with sharp and rounded corners, we again average the flow of both phases over the PSD of Fig. 2. Obviously other flow regimes will appear in pores of larger and smaller sizes than that of Fig. 13, but the general trend seems to hold: sharp corners pin interfaces and generally tend to reduce both  $\kappa_{r,i}$  relative to the rounded geometry. For the geometric and flow parameters tested, the sharp-cornered pores give  $\kappa_{r,w} = 0.023$  and  $\kappa_{r,n} = 0.42$ , while the round-cornered ones have  $\kappa_{r,w} = 0.069$  and  $\kappa_{r,n} = 1.34$ . In the latter, the

large relative permeability for the liquid phase is thanks to the lubrication of the liquid drops by the gas in the larger pores (Fig. 13*b*).

If the liquid bridge is initially next to the downstream end of the pore chamber (Fig. 13*c*), it wraps around the solid ridge and forms a continuous liquid film sealing some gas in the chamber. Meanwhile gas bubbles are transported in the middle in this bubble-slug regime. The difference between Fig. 13(*b*) and (*c*) is a special case of the hysteretic effect, where flow history affects the interfacial pattern that emerges eventually (Ahmadlouydarab et al., 2011). After averaging over the PSD, we obtain  $\kappa_{r,w} = 0.013$  and  $\kappa_{r,n} = 0.53$ , comparable to the sharp-cornered geometry and much below those of Fig. 13(*b*). As in Fig. 13(*a*), the liquid flow is hindered by wall friction and much of the gas is trapped. The lack of lubrication effect is the key factor in the lower  $\kappa_{r,i}$ .

#### 4. Conclusion

In this work we use pore-scale flow simulations to compute the relative permeability of a model porous medium and test the validity of the so-called extended Darcy's law for gas-liquid two-phase flow. The main conclusions can be summarized as follows.

- (*a*) The averaged gas and liquid flow rates both depend nonlinearly on the imposed pressure gradient. Thus the extended Darcy's law does not hold in the usual sense. Instead, it can be viewed as the definition of the relative permeabilities, which are complex functions of the geometric and flow parameters of the system.
- (*b*) The relative permeability of the wetting phase  $\kappa_{r,w}$  behaves more or less as expected from previous studies. It increases with the wetting-phase capillary number and the wetting-phase saturation, but decreases with the wettability of the pore surface and with the non-wetting-to-wetting viscosity ratio.
- (*c*) The relative permeability of the non-wetting phase  $\kappa_{r,n}$  has a much more complex behavior. It increases monotonically with the viscosity ratio, but exhibits non-monotonic dependence on the saturation and wetting angle. This is because the non-wetting phase tends to occupy the central part of the pore, and  $\kappa_{r,n}$  is much more sensitive to the interface morphology than  $\kappa_{r,w}$ . In particular, lubrication of the non-wetting phase by a cushion of the wetting phase is responsible for elevated  $\kappa_{r,n}$ ,

and loss of lubrication, e.g. when the non-wetting phase makes contact with the wall, leads to lower  $\kappa_{r,n}$ .

The strength of our work lies in the pore-scale resolution of the interfacial shape and its temporal evolution, as well as contact-line motion on the solid walls of the pore. Thus, the relative permeabilities can be directly related to the flow regimes and interfacial evolution in the two-phase flow. The role of interface pinning at sharp corners is highlighted, which leads to a dependence on flow history. The shortcoming of this work is the simplicity of its pore geometry. Periodic contraction (pore throat) and expansion (pore chamber) are accounted for, but connectivity among pores is neglected, as is the disordered nature of pore geometry in real porous media. This may have magnified the lubrication effect.

Comparisons with experimental and computational results in the literature show qualitative agreement in cases where a consistent trend exists. In other cases, previous papers have presented conflicting data. Our study adds more data to this situation, but cannot resolve the existing discrepancies. More studies under carefully controlled conditions are needed in the future.

**Acknowledgment:** This work was supported by an NSERC Strategic Project Grant. We thank G. H. (Bud) Homsy of UBC and John Shen of Palcan Fuel Cell Co. Ltd. for helpful discussions. JJF also acknowledges partial support from the Canada Research Chair program, NSERC’s Discovery Program and the Canada Foundation for Innovation.

## References

- Ahmadlouydarab, M., Liu, Z.S., Feng, J.J., 2011. Interfacial flows in corrugated microchannels: Flow regims, transitions and hysteresis. *Int. J. Multiphase Flow* 37, 1266–1276.
- Amaefule, J.O., Handy, L.L., 1982. The effect of interfacial tensions on relative oil/water permeabilities of consolidated porous media. *Soc. Pet. Eng. J.* 22, 371–381.
- Avraam, D.G., Payatakes, A.C., 1995a. Flow regimes and relative permeabilities during steady-state two-phase flow in porous media. *J. of Fluid Mech.* 293, 207–236.

- Avraam, D.G., Payatakes, A.C., 1995b. Generalized relative permeability coefficients during steady-state two-phase flow in porous media, and correlation with the flow mechanisms. *Transport in Porous Media* 20, 135–168.
- Avraam, D.G., Payatakes, A.C., 1999. Flow mechanics, relative permeabilities, and coupling effects in steady-state two-phase flow through porous media, the case of strong wettability. *Ind. Eng. Chem. Res.* 38, 778–786.
- Blunt, M.J., Jackson, M.D., Piri, M., Valvatne, P.H., 2002. Detailed physics, predictive capabilities and macroscopic consequences for pore-network models of multiphase flow. *Adv. Water Resour.* 25, 1069–1089.
- Dana, E., Skoczylas, F., 2002. Experimental study of two-phase flow in three sandstones. I measuring relative permeabilities during two-phase steady-state experiments. *Int. J. Multiphase Flow* 293, 1719–1736.
- Demond, A.H., Roberts, P.V., 1987. An examination of relative permeability relations for two-phase flow in porous media. *Water Resour. Bull.* 23, 617–628.
- Djilali, N., 2007. Computational modelling of polymer electrolyte membrane (PEM) fuel cells: Challenges and opportunities. *Energy* 32, 269–280.
- Ehrlich, R., 1993. Viscous coupling in two-phase flow in porous media and its effect on relative permeabilities. *Transport in Porous Media* 11, 201–218.
- Feng, J.J., Liu, C., Shen, J., Yue, P., 2005. An energetic variational formulation with phase field methods for interfacial dynamics of complex fluids: advantages and challenges, in: Calderer, M.C.T., Terentjev, E.M. (Eds.), *Modeling of Soft Matter*. Springer, New York, pp. 1–26.
- Gao, P., Feng, J.J., 2011. Spreading and breakup of a compound drop on a partially wetting substrate. *J. Fluid Mech.* 682, 415–433.
- Gustensen, A.K., Rothman, D.H., 1993. Lattice-Boltzmann studies of immiscible two-phase flow through porous media. *J. Geophys. Res.* 98, 6431–6441.
- Hao, L., Cheng, P., 2010. Pore-scale simulations on relative permeabilities of porous media by lattice Boltzmann method. *Int. J. Heat and Mass Transfer* 53, 1908–1913.

- Huang, H., Lu, X.Y., 2009. Relative permeabilities and coupling effects in steady-state gas-liquid flow in porous media: A lattice Boltzmann study. *Phys. Fluids* 21, 092104.
- Kalaydjian, F., 1990. Origin and quantification of coupling between relative permeabilities for two-phase flows in porous media. *Transport in Porous Media* 5, 215–229.
- Koido, T., Furusawa, T., Moriyama, K., 2008. An approach to modeling two-phase transport in the gas diffusion layer of a proton exchange membrane fuel cell. *J. of Power Sources* 175, 127–136.
- Li, H., Pan, C., Miller, C.T., 2005. Pore-scale investigation of viscous coupling effects for two-phase flow in porous media. *Phys. Rev. E* 72, 026705.
- Muskat, M., Meres, M.W., 1936. The flow of heterogeneous fluids through porous media. *Physics* 7, 346–363.
- Nguyen, V.H., Sheppard, A.P., Knackstedt, M.A., Pinczewski, W.V., 2006. The effect of displacement rate on imbibition relative permeability and residual saturation. *J. Petrol. Sci. Eng.* 52, 54–70.
- Ye, T., Shyy, W., Chung, J.N., 2001. A fixed-grid, sharp-interface method for bubble dynamics and phase change. *J. Comput. Phys.* 174, 781–815.
- Yiotis, A.G., Psihogios, J., Kainourgiakis, M.E., Papaioannou, A., Stubos, A.K., 2007. A lattice boltzmann study of viscous coupling effects in immiscible two-phase flow in porous media. *Colloids and Surfaces A: Physicochem. Eng. Aspects* 300, 35–49.
- Yue, P., Feng, J.J., 2011. Wall energy relaxation in the Cahn-Hilliard model for moving contact lines. *Phys. Fluids* 23, 012106.
- Yue, P., Feng, J.J., Liu, C., Shen, J., 2004. A diffuse-interface method for simulating two-phase flows of complex fluids. *J. Fluid Mech.* 515, 293–317.
- Yue, P., Feng, J.J., Liu, C., Shen, J., 2005. Diffuse-interface simulations of drop coalescence and retraction in viscoelastic fluids. *J. Non-Newtonian Fluid Mech.* 129, 163–176.
- Yue, P., Zhou, C., Dooley, J., Feng, J.J., 2008. Elastic encapsulation in bicomponent stratified flow of viscoelastic fluids. *J. Rheol.* 52, 1027–1042.

- Yue, P., Zhou, C., Feng, J.J., 2006a. A computational study of the coalescence between a drop and an interface in Newtonian and viscoelastic fluids. *Phys. Fluids* 18, 102102.
- Yue, P., Zhou, C., Feng, J.J., 2010. Sharp-interface limit of the Cahn-Hilliard model for moving contact lines. *J. Fluid Mech.* 645, 279–294.
- Yue, P., Zhou, C., Feng, J.J., Ollivier-Gooch, C.F., Hu, H.H., 2006b. Phase-field simulations of interfacial dynamics in viscoelastic fluids using finite elements with adaptive meshing. *J. Comput. Phys.* 219, 47–67.
- Zhang, F.Y., Yang, X.G., Wang, C.Y., 2006. Liquid water removal from a polymer electrolyte fuel cell. *J. Electrochem. Soc.* 153, A225–A232.
- Zhou, C., Yue, P., Feng, J.J., 2006. Formation of simple and compound drops in microfluidic devices. *Phys. Fluids* 18, 092105.
- Zhou, C., Yue, P., Feng, J.J., Ollivier-Gooch, C.F., Hu, H.H., 2010. 3D phase-field simulations of interfacial dynamics in Newtonian and viscoelastic fluids. *J. Comput. Phys.* 229, 498–511.